High-Speed Synchronous Reluctance Machine with Minimized Rotor Losses

Heath Hofmann, *Member, IEEE*, and Seth R. Sanders, *Member, IEEE*

***Abstract*—This paper presents a refined design of a high-speed synchronous reluctance machine with minimized eddy-current losses in the rotor. Design criteria are the ability of the rotor to withstand high speeds, ability to operate in vacuum, negligible zero-torque spinning losses, high reliability, high efficiency, and low manufacturing cost. The rotor of the synchronous reluctance machine consists of bonded sections of ferromagnetic and nonmagnetic steels. Finite-element code, incorporating rotor rotation, has been developed in MATLAB that calculates steady-state eddy currents (and losses) in the rotor. A stator iron and stator winding have been designed to minimize rotor losses, and two such prototype machines have been fabricated. Experimental results show an efficiency of 91% at a 10-kW 10 000-r/min operating point, and rotor losses less than 0.5% of input power.**

***Index Terms*—High-speed synchronous reluctance machine, steady-state finite-element analysis.**

I. Introduction

THERE is a need for a high-speed high-power low-cost electric machine with low rotor losses in applications such as the motor/alternator in a flywheel energy storage device. Such devices store energy by spinning a high-inertia flywheel at high rotational speeds. To reduce spinning losses, it is expected that the flywheel and the rotor of the motor/alternator will spin in vacuum, possibly supported by magnetic bearings. In such a setup, the main method of heat transfer through the vacuum is by blackbody radiation. To develop some intuition, a rotor temperature rise of 100 °C above a stator at a temperature of 100 °C can accomodate a blackbody heat radiation of only 84 W for the prototype dimensions discussed in the sequel. Hence, it is essential that the motor/alternator have low rotor losses.

We have designed a solid-rotor synchronous reluctance machine for flywheel applications, as introduced in [1]. A cross section of the rotor design is shown in Fig. 1. The rotor consists of bonded sections of ferromagnetic and nonmagnetic steels. As this rotor is not radially laminated, extreme care must be taken to ensure low rotor losses. Because the machine is synchronous, the rotor ideally sees dc flux. Rotor eddy currents are, therefore, only generated by harmonics, specifically, spatial stator winding and slot harmonics, and temporal stator current harmonics.

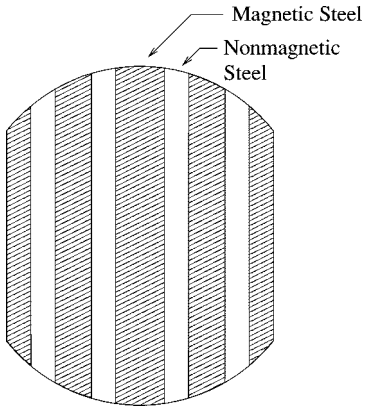

Fig. 1. Synchronous reluctance rotor design (cross section).

This paper presents a refined design of the synchronous reluctance machine, with minimized eddy-current losses in the rotor. First the advantages of synchronous reluctance machines with respect to permanent magnet machines for this particular application are discussed. Finite-element code, incorporating rotor rotation, has been developed to calculate steady-state eddy currents (and losses) in the rotor due to stator-current, stator-winding, and stator-slot harmonics. This paper will discuss this finite-element software and how its results guided the machine design. A stator iron and stator winding have been designed to minimize these rotor losses. Two prototype machines have been fabricated and tested, and experimental data are presented.

II. Machine Selection

A. Permanent-Magnet Machines

Most flywheel systems discussed in the literature use a permanent-magnet machine as the motor/alternator [1]–[4]. Permanent-magnet machines are a popular choice due to the high efficiency that can be obtained since no power loss is associated with machine excitation. There are, however, several disadvantages in using permanent-magnet machines for this particular application. High-energy-product permanent-magnet materials can be prohibitively expensive. They are also brittle and have marginal tensile strength and, thus, special care must be taken in rotor design so that they can withstand the large centrifugal forces experienced at high rotational speeds. Permanent magnets can demagnetize during excessive armature reaction, creating reliability concerns. Finally, permanent-magnet motors with iron in the stator experience significant "spinning" core loss, even when no power is being transferred through the motor.

Paper IPCSD 99–80, presented at the 1998 Industry Applications Society Annual Meeting, St. Louis, MO, October 12–16, and approved for publication in the IEEE TRANSACTIONS ON INDUSTRY APPLICATIONS by the Electric Machines Committee of the IEEE Industry Applications Society. Manuscript submitted for review July 14, 1999 and released for publication November 6, 1999.

H. Hofmann was with the Department of Electrical Engineering and Computer Science, University of California, Berkeley, CA 94720 USA. He is now with the Department of Electrical Engineering, The Pennsylvania State University, University Park, PA 16802 USA (e-mail: hofmann@engr.psu.edu).

S. R. Sanders is with the Department of Electrical Engineering and Computer Science, University of California, Berkeley, CA 94720 USA (e-mail: sanders@eecs.berkeley.edu).

Publisher Item Identifier S 0093-9994(00)02402-6.

0093–9994/00$10.00 © 2000 IEEE

The combination of these properties of permanent-magnet machines makes design of a low-cost high-reliability motor/alternator for flywheel applications particularly challenging.

B. Synchronous Reluctance Machines

Synchronous reluctance machines have the following advantages over permanent-magnet machines.

- There is no concern with demagnetization,
- The excitation field can be arbitrarily adjusted, allowing significant reduction of electromagnetic spinning losses at zero torque, and
- Synchronous reluctance machine rotors can be constructed entirely from high-strength low-cost materials.

The synchronous reluctance machine is typified by having a rotor whose structure is such that the inductance of the stator windings varies sinusoidally from a maximum value L_d (direct inductance) to a minimum value L_q (quadrature inductance) as a function of angular displacement of the rotor. A figure of merit for the synchronous reluctance machine is the ratio of direct inductance to quadrature inductance L_d/L_q. For example, the maximum achievable power factor $PF_{\max}$ of a synchronous reluctance machine is given by

$$PF_{\max} = \frac{L_d/L_q - 1}{L_d/L_q + 1}. \tag{1}$$

Higher L_d/L_q ratios yield higher power factors, which correspond to reduced I^2R losses and reduced voltampere ratings of the inverter driving the machine [5], [6], [15].

III. Finite-Element Analysis

In order to optimize the machine design to minimize rotor losses, we have developed finite-element code in MATLAB to characterize steady-state eddy currents in the rotor. The partial differential equation (PDE) for two-dimensional eddy-current analysis is as follows [7]:

$$\sigma \frac{\partial A_z}{\partial t} = \frac{\nabla^2 A_z}{\mu} + J_s \tag{2}$$

where A_z is the axial component of the magnetic vector potential, μ is the magnetic permeability, σ is the electrical conductivity, and J_s is the current density corresponding to applied currents in the stator windings. We note that, although the problem being simulated incorporates mechanical motion, we choose a Lagrangian representation of the stator and rotor coordinates and so velocity terms do not appear in the above formulation [8]. To keep the analysis tractable, linear constitutive relationships are assumed (i.e., constant $\sigma,\ \mu$).

By discretizing a cross section of the synchronous reluctance machine into a mesh and applying the linear Galerkin method [9], the PDE is reduced to a differential-algebraic equation (DAE)

$$\mathbf{S}\begin{bmatrix}\dot{\mathbf{a}}_s(t)\\ \dot{\mathbf{a}}_r(t)\end{bmatrix} + \mathbf{K}\begin{bmatrix}\mathbf{a}_s(t)\\ \mathbf{a}_r(t)\end{bmatrix} = \begin{bmatrix}\mathbf{I}_s(t)\\ \mathbf{0}\end{bmatrix} \tag{3}$$

where

$$\mathbf{S} = \begin{bmatrix}\mathbf{0} & \mathbf{0}\\ \mathbf{0} & \mathbf{S}_{rr}\end{bmatrix} \quad \mathbf{K} = \begin{bmatrix}\mathbf{K}_{ss} & \mathbf{K}_{sr}(t)\\ \mathbf{K}_{rs}(t) & \mathbf{K}_{rr}\end{bmatrix}$$

$\mathbf{a}_s$ and $\mathbf{a}_r$ are vectors containing the nodal magnetic vector potentials for the stator and rotor, $\mathbf{S}_{rr}$ is a matrix representing the conductivity of the rotor elements, the $\mathbf{K}_{xy}$ are matrices representing the magnetic permeability of elements, and $\mathbf{I}_s(t)$ is a vector which represents the enforced currents in the stator windings. The matrices $\mathbf{K}_{rs}(t)$ and $\mathbf{K}_{sr}(t)$ are functions of time because they incorporate the relative position of the rotor with respect to the stator. Inspection of (3) reveals an expression for $\mathbf{a}_s$

$$\mathbf{a}_s = \mathbf{K}_{ss}^{-1}(\mathbf{I}_s - \mathbf{K}_{sr}(t)\mathbf{a}_r) \tag{4}$$

which, in turn, allows us to write an ordinary differential equation (ODE) for $\mathbf{a}_r$

$$\begin{aligned}\dot{\mathbf{a}}_r(t) = &-\mathbf{S}_{rr}^{-1}[\mathbf{K}_{rr} - \mathbf{K}_{rs}(t)\mathbf{K}_{ss}^{-1}\mathbf{K}_{sr}(t)]\mathbf{a}_r(t)\\ &- \mathbf{S}_{rr}^{-1}\mathbf{K}_{rs}(t)\mathbf{K}_{ss}^{-1}\mathbf{I}_s(t).\end{aligned} \tag{5}$$

We will use this ODE formulation in the following discussion of steady-state operation. Integration of the DAE in (3) is performed using the backward Euler method. Rotational motion is taken into account by spacing the nodes equidistant along the surface of the rotor, and choosing our time step such that it corresponds to a circumferential displacement of the rotor equivalent to the distance between two nodes on the rotor surface. Hence, after each time step, we rotate the rotor by reassigning nodal relationships at the stator–rotor boundary, which is done simply by shifting rows and columns of $\mathbf{K}_{sr}(t)$ and $\mathbf{K}_{rs}(t)$, respectively.

A. Steady-State Analysis Using Generalized Minimum Residual Method (GMRES)

Computing rotor losses requires knowledge of the steady-state operation of the machine. This could be achieved by running a transient simulation until the natural dynamics of the system decay to an acceptable level. However, this is a time-intensive and computationally intensive approach. Instead, we use an approach developed in [10]. Returning to the ODE problem (5), the solution to the rotor magnetic vector potential can be written in the following form [11]:

$$\mathbf{a}_r(t) = \Phi(t,0)\mathbf{a}_r(0) + \int_0^t \Phi(t,\tau)\mathbf{u}(\tau)\,d\tau \tag{6}$$

where $\Phi(t,0)$ is the state transition matrix of (5) and

$$\mathbf{u}(t) = -\mathbf{S}_{rr}^{-1}\mathbf{K}_{rs}(t)\mathbf{K}_{ss}^{-1}\mathbf{I}_s(t). \tag{7}$$

For a steady-state solution, we wish to achieve the same rotor magnetic vector potential after one period of rotation T

$$\mathbf{a}_r(T) = \mathbf{a}_r(0). \tag{8}$$

Using this relation and (6) yields the following system of equations:

$$(\Phi(T,0) - \mathbf{I})\mathbf{a}_r(0) = \int_0^T \Phi(T,\tau)\mathbf{u}(\tau)\,d\tau. \tag{9}$$

This equation can, therefore, be solved for $\mathbf{a}_r(0)$ using a linear solver. However, typical solvers such as Gaussian elimination would require computation of the state transition matrix $\Phi(T,0)$, which would be computationally intensive. Instead, we use an iterative method, namely, GMRES [10], [12]. This method solves $\mathbf{Ax} = \mathbf{b}$ without knowledge of $\mathbf{A}$. All that is necessary is the ability to generate the matrix–vector products $\mathbf{Ax}$. The matrix–vector product $\Phi(T,0)\mathbf{x}$ is generated by integrating the system (5) with initial condition $\mathbf{x}$ and no input, i.e., $\mathbf{u}(t) = 0$, for one period. Once $\mathbf{a}_r(0)$ is calculated, the entire steady-state response can be calculated by integrating (5). GMRES can also be used to calculate steady-state solutions of nonlinear systems, as discussed in [10].

B. Rotor Losses

To calculate rotor losses, we perform a discrete Fourier transform (DFT) of the steady-state response $\mathbf{a}_r(t)$ in order to acquire the complex Fourier coefficients $\mathbf{A}_r^i = \mathbf{A}_r(\omega_i)$, where the ω_i correspond to the ith multiples of the fundamental rotational frequency of the rotor. Eddy-current rotor losses are then calculated by first integrating the square of the eddy-current magnitude over each element

$$\begin{aligned}\int_{S_n} & \|J_e(\omega_i)\|^2\, dS \\ &= \omega_i^2\sigma_n^2 \int_{S_n} \|\mathbf{A}_r^i\|^2\, dS \\ &= \omega_i^2\sigma_n^2 \frac{S_n}{6}\Big[|\mathbf{A}_{rn1}^i|^2 + |\mathbf{A}_{rn2}^i|^2 + |\mathbf{A}_{rn3}^i|^2 \\ &\quad + \frac{1}{2}\left(\mathbf{A}_{rn1}^i\overline{\mathbf{A}}_{rn2}^i + \mathbf{A}_{rn2}^i\overline{\mathbf{A}}_{rn1}^i\right. \\ &\quad + \mathbf{A}_{rn1}^i\overline{\mathbf{A}}_{rn3}^i + \mathbf{A}_{rn3}^i\overline{\mathbf{A}}_{rn1}^i + \mathbf{A}_{rn2}^i\overline{\mathbf{A}}_{rn3}^i \\ &\quad \left.+ \mathbf{A}_{rn3}^i\overline{\mathbf{A}}_{rn2}^i\right)\Big] \end{aligned} \tag{10}$$

where $\mathbf{A}_{rn1}, \mathbf{A}_{rn2}$, and $\mathbf{A}_{rn3}$ correspond to the magnetic vector potential at the nodes of the nth triangular finite element of the rotor, S_n is the area of the nth element, and σ_n is the electrical conductivity of the nth element, and then summing the resistive losses of all elements at all frequencies

$$P_{rotor} = \sum_i \sum_{n=1}^{N_r} \frac{\ell_s}{2\sigma_n} \int_{S_n} \|J_e(\omega_i)\|^2\, dS \tag{11}$$

where ℓ_s is the stack length.

C. Finite-Element Analysis Results

The finite-element mesh of the prototype design is shown in Fig. 2. As the eddy currents appear only on the rotor surface, a very fine mesh is constructed on the surface of the rotor to capture these dynamics. This surface mesh can be seen in Fig. 3.

A steady-state response was calculated for the prototype design at a 60-kW 48 000-r/min operating point using the finite-element tool. Fig. 3 displays eddy currents on the rotor surface corresponding to the 72nd harmonic, which are generated by the stator slots. A breakdown of eddy-current rotor losses as a function of harmonic frequency is presented in Fig. 4. Simulations suggest that rotor losses in our design will be ≈ 300 W when operating at a 60-kW 48 000-r/min operating point. Using the blackbody heat dissipation of 84 W discussed in Section I, this would allow the machine to operate at full power with a duty cycle of 28%. When coasting at 48 000 r/min and zero torque, but at rated flux (0.08 Wb), rotor losses are estimated to be approximately 50 W.

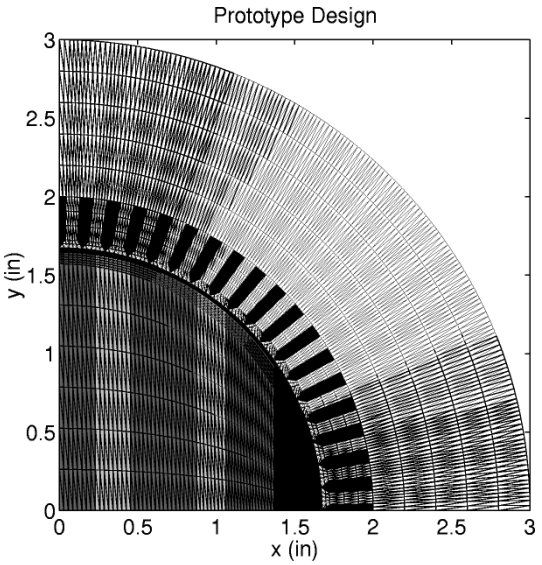

Fig. 2. Finite-element mesh of prototype design.

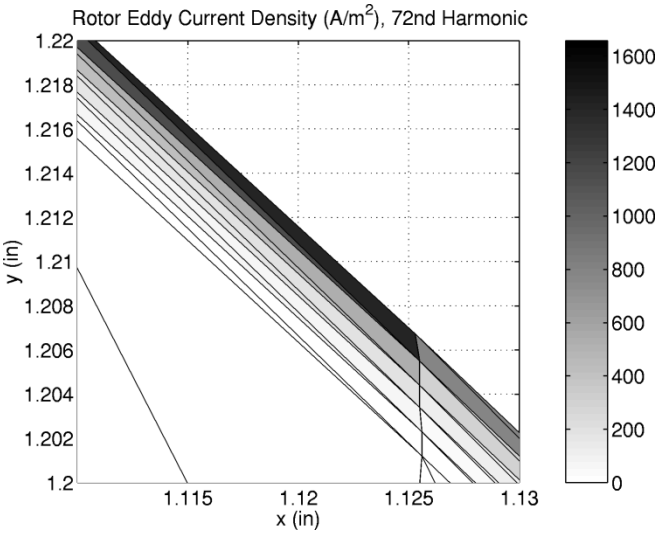

Fig. 3. Plot of the 72nd harmonic eddy-current magnitudes on rotor surface (60-kW 48 000-r/min operating point). Design has 72 stator teeth.

IV. Design Strategy

A. Base-Case Machine Design

This section discusses how the finite-element results influenced the synchronous reluctance machine design. To qualitatively discuss the effects of design changes, we use a base-case machine design and operating point, as defined in Table I. We note that this design is slightly different than the design of our prototype. In all simulations, we assume relative permeabilities $\mu_r = 1000$ for the ferromagnetic steels and $\mu_r = 1$ for the nonmagnetic steels. The windings for the base case design are

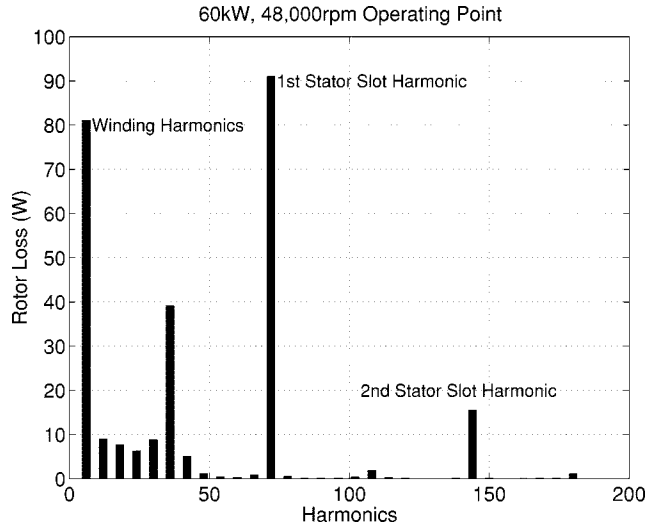

Fig. 4. Eddy-current losses in rotor as a function of harmonic frequency (60-kW 48 000-r/min operating point).

designed to minimize rotor losses due to winding harmonics, as will be discussed in Section IV-C. The rotor dimensions remain constant in all simulations.

B. Rotor Design

Primary design criteria for the rotor are:

- choice of thicknesses of the ferromagnetic and nonmagnetic sections;
- choice of materials for the ferromagnetic and nonmagnetic sections.

The thicknesses of the sheets are chosen to optimize the L_d/L_q ratio of the machine, as discussed in [1].

The choice of steels for the rotor magnetic and nonmagnetic sheets depends on criteria besides their magnetic properties. The materials must have high yield strength to withstand the large centrifugal forces experienced at high speeds. Also of interest is the electrical resistivity ρ of the materials. Table II shows the rotor losses for different materials, as calculated by finite-element analysis. The ferromagnetic materials studied are 3% silicon–iron ($\rho = 43\ \mu\Omega \cdot$ m) and 4140 ($\rho = 43\ \mu\Omega \cdot$ m), an inexpensive carbon steel. The nonmagnetic materials studied are Nitronic 50, a specialty stainless steel ($\rho = 82\ \mu\Omega \cdot$ m), and aluminum–bronze ($\rho = 12\ \mu\Omega \cdot$ m). The Nitronic 50 steel was chosen for its high tensile strength (120 000 lb/in^2). These results suggest that it is desirable to use materials with higher resistivities.

C. Stator Design

The key design criteria for the stator were to achieve a power rating of 60 kW over the speed range of 24 000–48 000 r/min, while achieving an efficiency of $\approx$ 95%. While attaining these performance goals, it is also necessary to minimize rotor losses. As discussed in the introduction, rotor losses are generated by spatial stator winding and slot harmonics, and temporal stator current harmonics. The next two sections focus on minimizing the winding and slot harmonics experienced by the rotor.

TABLE I
BASE CASE SYNCHRONOUS RELUCTANCE MACHINE DESIGN

No. Stator Teeth:	60
Stator Slot Configuration:	Closed
Stack length:	6 in.
Air gap:	0.025 in.
Rotor Diameter:	3.25 in
Rotor Ferromagnetic Steel:	4140
Rotor Nonmagnetic Steel:	Nitronic 50
Output Power:	$60kW$
Operating Speed:	$48,000rpm$

TABLE II
ROTOR LOSSES FOR DIFFERENT ROTOR MATERIALS

Rotor Materials	Rotor Losses
SiFe, Nitronic 50 (Base Case)	410W
4140, Nitronic 50	443W
SiFe, AlBr	540W

1) Winding Harmonics: The magnetomotive force (MMF) a stator winding phase exerts on the rotor at an angle θ can be represented in terms of odd-numbered spatial harmonics

$$MMF(\theta) = I\sum_{i=1}^{\infty} a_{2i-1}\cos(2i-1)\theta \tag{12}$$

where I is the instantaneous current in the phase winding. For a three-phase two-pole winding structure with sinusoidal currents of frequency ω and peak value I_{pk}, with the rotor spinning at the same frequency ω, the total MMF seen by the rotor at an angle θ_r can be shown to have the form given by

$$MMF_{\text{tot}}(\theta_r, t) = \frac{3I_{pk}}{2}\left[a_1\cos\theta_r + \sum_{i=1}^{\infty} a_{6i-1} \cdot \cos((6i-1)\theta_r + 6i\omega t) + a_{6i+1} \cdot \cos((6i+1)\theta_r + 6i\omega t)\right]. \tag{13}$$

The rotor sees the $(6i-1)$ and $(6i+1)$ spatial harmonics of the stator windings aliased into $6i$ time harmonics. Using (13), a winding structure has been designed to minimize rotor losses for a given fundamental MMF. In this design, we assume eddy currents developed in the rotor completely cancel the MMF harmonics, taking into account the skin effect at different frequencies.

TABLE III
ROTOR LOSSES OF VARYING WINDING CONFIGURATIONS

Winding Configuration	Rotor Losses
Sinusoidal (Ideal):	228W
Optimized (Base Case):	410W
Concentrated:	464W

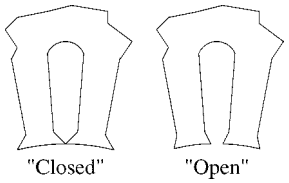

Fig. 5. Stator slot designs.

TABLE IV
ROTOR LOSSES OF CLOSED SLOTS VERSUS OPEN SLOTS

Stator Slot Configuration	Rotor Losses
Closed Slots (Base Case):	410W
Open Slots:	1,568W

TABLE V
ROTOR LOSSES AS FUNCTION OF SLOT NUMBER. STATOR WINDINGS ARE SINUSOIDALLY DISTRIBUTED IN SLOTS TO ELIMINATE WINDING HARMONICS

# Stator Slots	Rotor Losses
30 Slots:	1297W
60 Slots:	228W
90 Slots:	211W

Rotor losses for various winding schemes are presented in Table III. The "sinusoidal" winding scheme is an ideal, non-physical scheme in which each slot has a fraction of all three phases, distributed sinusoidally according to the angular location of the slot. In the "concentrated" winding structure, each half of a phase is placed in contiguous slots.

2) Slot Harmonics: This section analyzes the effect of stator slots on rotor losses. The focus is on two aspects: the number of stator slots, and whether the slots are closed or open, as shown in Fig. 5. Finite-element analysis reveals that the rotor losses are dramatically reduced if the stator slots are closed, as shown in Table IV. In the open-slot design simulated, the stator teeth faces comprise 2/3 of the total surface area.

In order to achieve sufficiently low rotor loss, our prototype design incorporates closed stator slots. Most machines have open stator slots in order to assist in winding the stator coils. To avoid this problem in construction of the prototype, we use copper bus bar instead of wire, as copper bars can be inserted more easily into the stator slots. As each bus bar represents one turn of a winding, this approach places a practical limit on the number of turns in a phase. However, because this is a high-speed machine, the number of turns comprising the stator windings must be low to keep the voltage rating reasonable, hence this is a practical solution. The windings were assembled in a ring-winding configuration, as shown in Fig. 9.

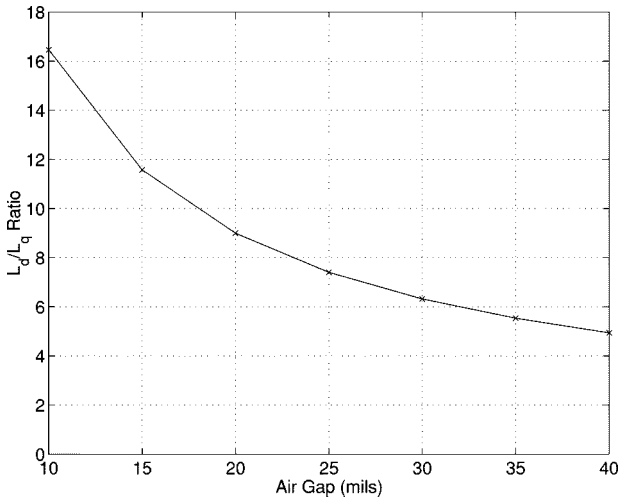

Fig. 6. Calculated L_d/L_q ratio of synchronous reluctance as function of air gap. Calculations performed using a magnetic circuit model presented in [1].

Simulations also suggest that rotor losses are reduced if the number of slots is increased, as shown in Table V. To remove the effect of winding harmonics in this comparative analysis, currents are assigned in the slots in an ideal sinusoidal fashion, as discussed in Section IV-C–1. All of the designs have closed stator slots.

D. Air Gap

Synchronous reluctance machines are typically designed with small air gaps, so as to improve the L_d/L_q ratio. Fig. 6 shows the L_d/L_q ratio of the base case design as a function of air gap, calculated using a magnetic circuit model originally presented in [1], and further refined in [13]. However, as shown in Fig. 7, small air gaps can also cause higher rotor losses.

E. Analytical Expressions for Rotor Losses

Simplified analytical expressions for the rotor losses, derived from models presented in [8], support these finite-element results. The derivation and explanation of these expressions would take a significant amount of space, however, and, therefore, the interested reader is referred to [13].

V. EXPERIMENTAL SETUP

A. Prototype Fabrication

A design incorporating the considerations discussed in Section IV is presented in Table VI. Two prototype machines of this design have been fabricated. The rotors consist of layers of 4140 (magnetic) and Nitronic 50 (nonmagnetic) steels bonded together by brazing (see Fig. 8). An amorphous nickel foil was used for the braze. Tensile strength tests performed on a sample of the brazed material show the bond can withstand up to 58 000 lb/in^2. Results of mechanical finite-element analysis suggest the rotor experiences a Von Mises stress of 22 000 lb/in^2 at 48 000

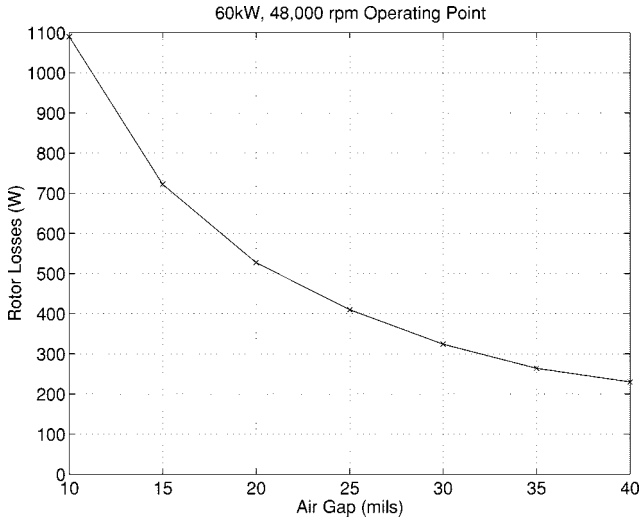

Fig. 7. Rotor losses versus air gap.

TABLE VI
SYNCHRONOUS RELUCTANCE MOTOR/ALTERNATOR PROTOTYPE DESIGN SUMMARY

Parameter	Value
Stator Outer Diameter:	6.5 in.
Stack Length:	6.0 in.
Stator Laminations:	M-15 Silicon Steel (14 mil)
# Stator Slots:	72
# Phases :	3
# Turns/Phase:	12
Measured DC Phase Resistance:	18 $m\Omega$
Rotor Diameter (d):	3.25 in.
Rotor Magnetic Steel:	4140
Rotor Nonmagnetic Steel:	Nitronic 50
Air Gap:	0.025 in.
# Poles:	2

r/min, yielding a safety factor of approximately 2.6. As mentioned earlier, a higher resistivity for the ferromagnetic steel would be preferred, such as that of silicon–iron, but sheets of silicon–iron of the desired thickness were not readily available.

The stator windings were constructed using copper bus bars in a ring-winding configuration (see Fig. 9). The laminations were laser cut, and then welded together along the outer diameter to make the stack. The lamination was designed such that

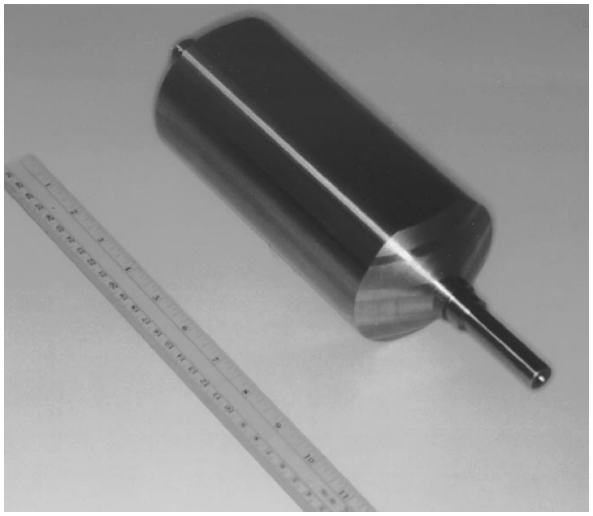

Fig. 8. Prototype rotor, consisting of brazed sheets of 4140 (magnetic) and Nitronic 50 (nonmagnetic) steels.

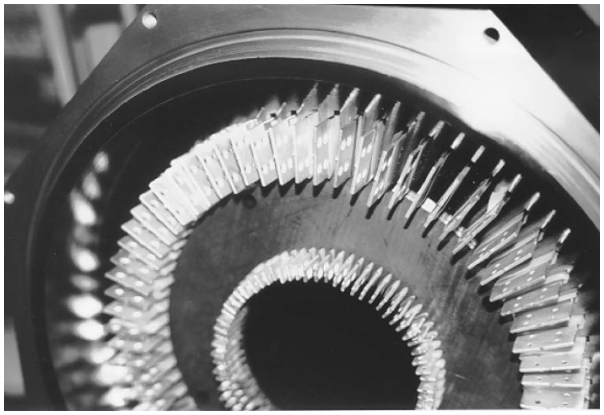

Fig. 9. Prototype stator with copper bus bar. Teflon sheet is used as a slot lining. The copper bus bar is coated with silver to minimize contact resistance and is wrapped in Kapton tape for insulation. A ring-winding configuration is used.

the stator teeth meet at a point. This is done to minimize rotor losses, as discussed previously. However, when manufactured, there must either be a small amount of material connecting the teeth, or a small gap between the teeth. The prototype laminations have an approximately 15-mil spacing between the tips of the stator teeth, as shown in Fig. 10. Deep-groove ball bearings with ceramic balls and a high-speed grease are used. The two prototype machines are connected at the shaft with a flexible coupling. The aluminum stator housings can be sealed together and used as a vacuum chamber. An infrared temperature sensor is mounted on the chamber, and is directed at the flexible shaft coupling. Electrical connections are made to the machines via brass bolts through holes in the endplates. The finished setup is shown in Fig. 11.

A schematic of the experimental test setup is shown in Fig. 12. Two high-efficiency inverters, connected to a common voltage bus, have been constructed to drive the machines. A three-phase LC filter at the output of each inverter removes pulsewidth modulation (PWM) harmonics, exposing the machines to relatively ideal voltages and currents. Driving one machine as a motor and the other as a generator causes power to flow in a loop. An

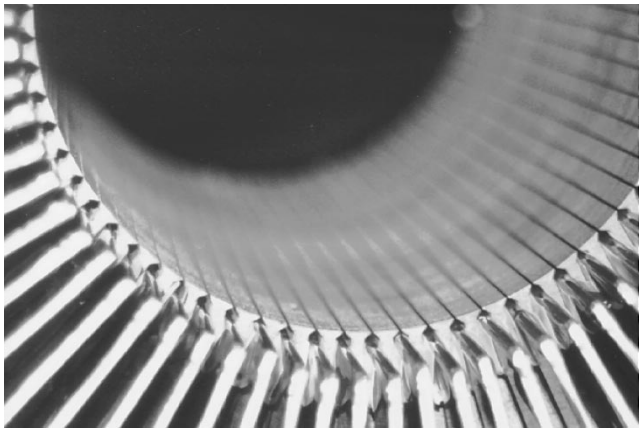

Fig. 10. Closeup of prototype stator, showing small gap between stator teeth.

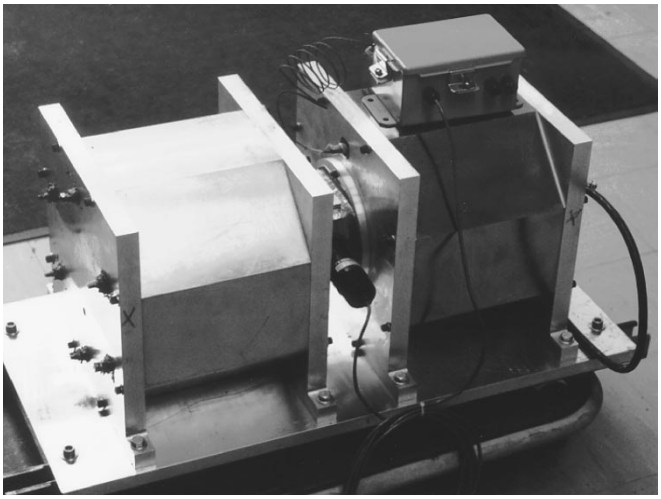

Fig. 11. Machine housings, housing coupling used to create a vacuum chamber, and infrared sensor used to measure rotor temperature. Electrical connections made to machines via brass bolts in holes through endplates.

external power source is used to supply the necessary power to keep the machines at a given steady-state operating point. Measurement of this dc input power allows accurate assessment of the total system losses. A stator-flux-oriented torque control scheme is used to drive the machines, as presented in [14].

B. Experimental Results

Fig. 13 displays measured two-phase steady-state stator currents in the stator-flux reference frame, with a stator-flux magnitude of 0.08 Wb and a rotational velocity of 4000 r/min. Each point corresponds to a different torque value. Values of positive and negative i^e_{sq} correspond to motor and generator operation, respectively. Direct and quadrature inductances L_d and L_q were then extracted from this data by performing a least-squares curve fitting of the experimental data with the analytical model. To achieve a better curve fit, a core-loss conductance G_c was added to the model in parallel with the machine inductance. The resulting parameters are shown in Table VII.

Further data was taken at 10 000 r/min with a commanded stator-flux magnitude of 0.085 Wb and a commanded torque of 10 N·m, resulting in a 10-kW operating point. The results are

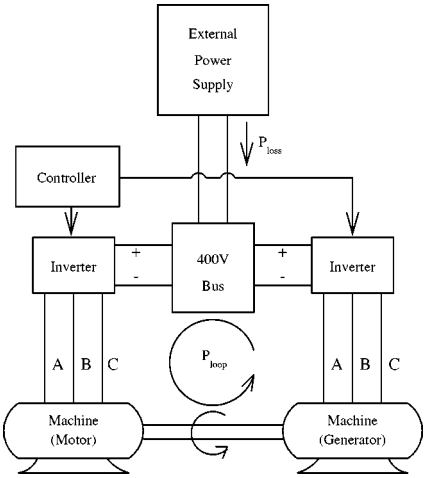

Fig. 12. Experimental setup.

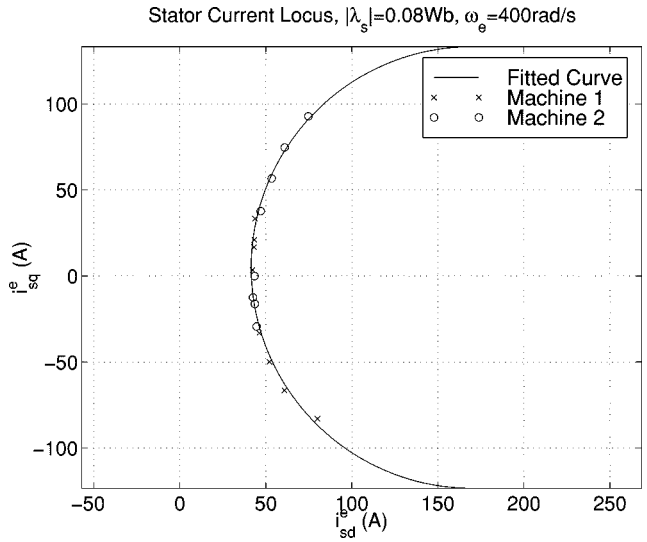

Fig. 13. Two-phase stator current locus in stator flux reference frame ($\|\lambda_s\| = 0.08$ Wb, 4000 r/min). Experimental data and least-squares curve fitting to analytical model.

TABLE VII
MACHINE PARAMETERS CALCULATED BY LEAST-SQUARES CURVE FITTING OF DATA IN Fig. 13 (0.08-Wb 4000-r/min OPERATING POINT)

Machine Parameter	**Value**
Direct Inductance L_d:	$1.93mH$
Quadrature Inductance L_q:	$0.27mH$
L_d/L_q Ratio:	7.2
Core Loss Conductance G_c:	$0.154mhos$

reported in Table VIII. We note that these losses include other losses besides core and copper losses, such as drag losses due to the air drag and the mechanical bearings. Rundown experiments on the system suggest these drag losses are approximately 175 W at 10 000 r/min. Although the machine was not tested at

TABLE VIII
EXPERIMENTAL RESULTS (10 000-r/min 10-kW OPERATING POINT)

Rotational Velocity:	$10,000rpm$
Commanded Stator Flux:	$0.085Wb$
Commanded Torque:	$10N \cdot m$
Electrical Power into Machine 1:	$10.64kW$
Electrical Power out of Machine 2:	$8.77kW$
Total Machine Losses:	$1.87kW$
Total Losses in System:	$2.77kW$
Inverter Losses:	$900W$
Round-Trip Efficiency of Machines:	82.4%
Approx. Efficiency of Each Machine:	**91.2%**

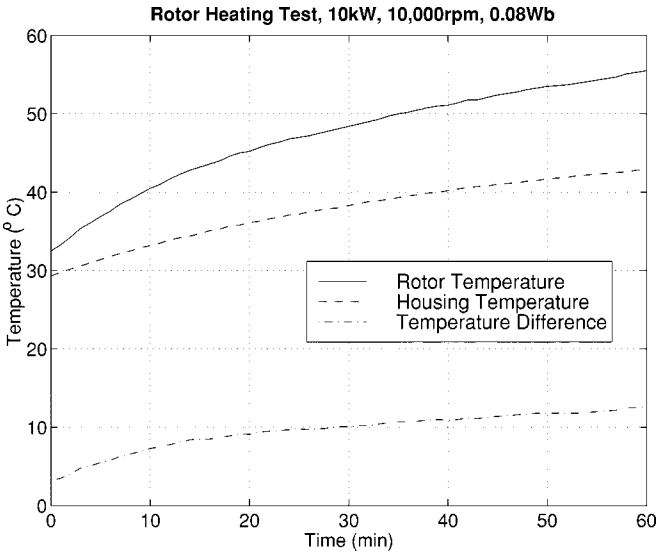

Fig. 14. Rotor heating experiment (10 000 r/min, 10 N·m, 0.08 Wb).

the 48 000-r/min operating point, spin tests were conducted at speeds up to 24 000 r/min without difficulty.

C. Rotor Heating

One of the most important design goals was to minimize losses in the rotor. In order to determine the amount of heat being generated in the rotor, the following experiment was performed. The motor/generator pair was run at 10 000 r/min, 10.0 kW for 1 h with the machine housing evacuated to <1 torr. The measured machine efficiency at this operating point at the end of the experiment was 88%. Temperature measurements were taken on the shaft coupling (using an infrared thermometer), and on the machine housing every 5 min. Rotor temperature (T_R), housing temperature (T_H), and their difference ($T_{\text{diff}} = T_R - T_H$) are shown in Fig. 14.

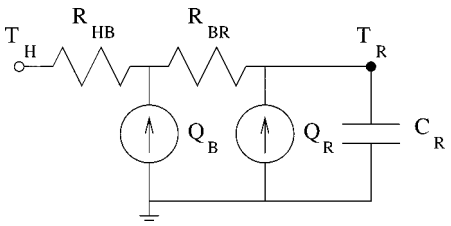

Fig. 15. Thermal circuit used to determine rotor losses.

TABLE IX
THERMAL PARAMETERS

Parameter	Description
R_{HB}	Housing-Bearing Therm. Resistance
R_{BR}	Bearing-Rotor Therm. Resistance
C_R	Heat Capacity of Rotor
Q_R	Rotor Heat Source
Q_B	Bearing Heat Source

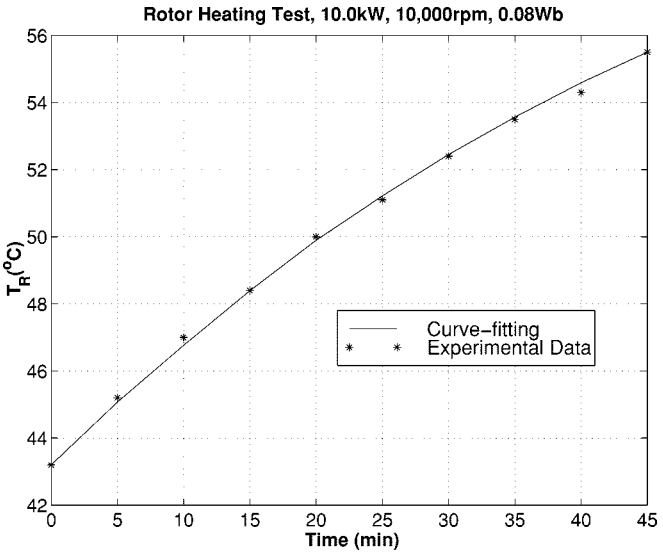

Fig. 16. Curve fitting of estimated parameters to experimental data for T_r (10 kW, 10 000-r/min 0.08-Wb operating point).

The thermal model used to estimate rotor losses is shown in Fig. 15, with its parameters described in Table IX. In this model, it is assumed that all heat leaving the rotor travels through the bearing, in other words, heat transfer via blackbody radiation is negligible. The blackbody radiation leaving the rotor at a rotor temperature of 55 °C and a stator temperature of 43 °C (the rotor and housing temperatures, respectively, at the end of the above experiment) is estimated to be 5 W. While not negligible, this

heat transfer turns out to be approximately an order of magnitude less than the total estimated rotor losses, hence, this is a reasonable assumption.

The rotor heat capacity $C_r = 3200$ J/°C can be calculated from the volume and material properties of the rotor. Based on the thermal model, it can be shown that the dynamics of the rotor temperature are represented by the expression

$$\begin{aligned} \frac{d}{dt}T_R &= aT_{\text{diff}} + b \\ a &= \frac{1}{(R_{HB}+R_{BR})C_R} \\ b &= \frac{1}{C_R}\left(Q_R + Q_B\frac{R_{HB}}{R_{HB}+R_{BR}}\right) \\ T_{\text{diff}} &= T_R - T_S. \end{aligned} \tag{14}$$

Discretization of (14), using trapezoidal integration, results in the following expression:

$$\frac{T_R^{k+1}-T_R^k}{h} = \frac{a}{2}\left(T_{\text{diff}}^{k+1}+T_{\text{diff}}^k\right)+b \tag{15}$$

where h is the time interval between data points. Using the experimental data and (15), least-squared-error values of the coefficients a and b are determined. Only the final 45 min of data are used in order to reduce the effects of startup transients on the results. A curve fitting of T_R using the calculated parameters is shown in Fig. 16. Based on this curve fitting, the heat generated by a rotor is estimated to be approximately 45 W, or less than 0.5% of the input power. Finite-element analysis performed at the same operating point yielded losses of 25 W. Possible explanations for this discrepancy are unmodeled effects, such as stator current harmonics, the small gap between the stator teeth, and the assumptions of linear material properties. Nevertheless, the goal of reducing rotor losses has been satisfactorily achieved.

VI. Conclusion

A high-speed synchronous reluctance machine with minimized rotor losses has been designed, fabricated, and tested. Finite-element code has been developed to characterize eddy-current losses in the rotor, thereby aiding the design process. Experimental results show that good efficiency and low rotor heating are achieved by the prototype machines.

References

[1] H. Hofmann and S. R. Sanders, "Synchronous reluctance motor/alternator for flywheel energy storage systems," in *Proc. 1996 IEEE Power Electronics in Transportation Workshop*, 1996, pp. 199–206.

[2] Abacus Technology Corporation, "Technology assessments of advanced energy storage systems for electric and hybrid vehicles," U.S. Department of Energy Office of Transportation Technologies, Tech. Rep. DE93-014395, NTIS Document, Apr. 1993.

[3] Lawrence Livermore Laboratory, "Feasibility of electromechanical batteries for electric vehicles," U.S. Department of Commerce, Tech. Rep. DE92-015172, NTIS Document, May 1992.

[4] P. P. Acarnley, B. C. Mecrow, J. S. Burdess, J. N. Fawcett, J. G. Kelly, and P. G. Dickinson, "Design principles for a flywheel energy store for road vehicles," in *Conf. Rec. 30th IEEE-IAS Annu. Meeting*, 1995, pp. 672–678.

[5] S. A. Nasar, I. Boldea, and L. E. Unnewehr, *Permanent Magnet, Reluctance, and Self-Synchronous Motors*. Boca Raton, FL: CRC Press, 1993.

[6] T. A. Lipo, A. Vagati, L. Malesani, and T. Fukao, "Synchronous reluctance motors and drives—A new alternative," presented at the 26th IEEE-IAS Annu. Meeting, Oct. 1992.

[7] H. H. Woodson and J. R. Melcher, *Electromechanical Dynamics*. New York: Wiley, 1968.

[8] J. R. Melcher, *Continuum Electromechanics*. Cambridge, MA: MIT Press, 1981.

[9] J. N. Reddy, *An Introduction to the Finite Element Method*. New York: McGraw-Hill, 1993.

[10] R. Telichevesky, K. S. Kundert, and J. K. White, "Efficient steady-state analysis based on matrix-free krylov-subspace methods," in *Proc. 32nd Design Automation Conf.*, 1995, pp. 480–484.

[11] T. Kailath, *Linear Systems*. Englewood Cliffs, NJ: Prentice-Hall, 1980.

[12] Y. Saad and M. H. Schultz, "Gmres: A generalized minimal residual algorithm for solving nonsymmetric linear systems," *SIAM J. Sci. Stat. Comput.*, vol. 7, no. 3, pp. 840–855, July 1986.

[13] H. Hofmann, "High-speed synchronous reluctance machine for flywheel applications," Ph.D. dissertation, Dep. Elect. Eng. Comput. Sci., Univ. California, Berkeley, Dec. 1998.

[14] H. Hofmann and S. R. Sanders, "Optimal efficiency controller for synchronous reluctance flywheel drive," in *Proc. INTELLEC'98*, 1998, pp. 724–731.

[15] W. Fong and J. Htsui, "New type of reluctance motor," *Proc. Inst. Elect. Eng.*, pp. 545–551, Mar. 1970.

[16] F. Leonardi, T. Matsuo, and T. A. Lipo, "Iron loss calculation for synchronous reluctance machines," in *Proc. 1996 Int. Conf. Power Electronics, Drives and Energy Systems for Industrial Growth*, pp. 307–312.

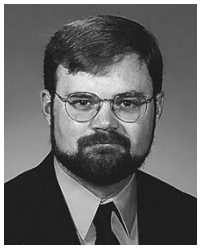

Heath Hofmann (S'89–M'92) received the B.S. degree in electrical engineering from the University of Texas, Austin, and the M.S. and Ph.D. degrees in electrical engineering from the University of California, Berkeley, in 1992, 1997, and 1998, respectively.

In 1999, he joined the Electrical Engineering Department, The Pennsylvania State University, University Park, where he is currently an Assistant Professor. His research interests are in electromechanical systems, power electronics, and numerical simulation. Current research topics are the design of high-speed electric machines, field-oriented control techniques, piezoelectric power generation, steady-state finite-element analysis, and modeling of ferrous materials. He is the primary coauthor of several journal papers on electric machine design and control.

Dr. Hofmann was a recipient of a Prize Paper Aaward from the Electric Machines Committee at the 1998 IEEE Industry Applications Society Annual Meeting.

Seth R. Sanders (M'87) received S.B. degrees in electrical engineering and physics and the S.M. and Ph.D. degrees in electrical engineering from Massachusetts Institute of Technology, Cambridge, in 1981, 1985, and 1989, respectively.

He was a Design Engineer at the Honeywell Test Instruments Division, Denver, CO. Since 1989, he has been with the Department of Electrical Engineering and Computer Science, University of California, Berkeley, where he is currently an Associate Professor. His research interests include variable-speed ac motor drive systems, high-frequency power conversion circuits and components, and nonlinear circuit and system theory as related to the power electronics field. During the 1992–1993 academic year, he was on industrial leave with National Semiconductor, Santa Clara, CA.

Dr. Sanders was the recipient of the National Science Foundation Young Investigator Award in 1993. He has served as Chair of the IEEE Technical Committee on Computers in Power Electronics and as a Member-At-Large of the IEEE PELS AdCom.